





# Comparative determinant quantum Monte Carlo study of the acoustic and optical variants of the Su-Schrieffer-Heeger model

Sohan Malkaruge Costa , Benjamin Cohen-Stead , Andy Tanjaroon Ly , James Neuhaus , and Steven Johnston 

*Department of Physics and Astronomy, The University of Tennessee, Knoxville, Tennessee 37996, USA*

*and Institute of Advanced Materials and Manufacturing, The University of Tennessee, Knoxville, Tennessee 37996, USA*



(Received 20 July 2023; revised 7 September 2023; accepted 4 October 2023; published 19 October 2023)

We compare the acoustic Su–Schrieffer–Heeger (SSH) model with two of its optical variants where the phonons are defined on either on the sites or bonds of the system. First, we discuss how to make fair comparisons between these models in any dimension by ensuring their dimensionless coupling  $\lambda$  and relevant phonon energies are the same. We then use determinant quantum Monte Carlo to perform nonperturbative and sign-problem-free simulations of all three models on one-dimensional chains at and away from half-filling. By comparing the results obtained from each model, we demonstrate that the optical and acoustic models produce near identical results within error bars for suitably chosen phonon energies and  $\lambda$  at half-filling. In contrast, the bond model has quantitatively different behavior due to its coupling to the  $\mathbf{q} = 0$  phonon mode. These differences also manifest in the total length of the chain, which shrinks for the bond model but not for the acoustic and optical models when  $\lambda \neq 0$ . Our results have important implications for quantum Monte Carlo modeling of SSH-like interactions, where these models are sometimes regarded as being interchangeable.

DOI: [10.1103/PhysRevB.108.165138](https://doi.org/10.1103/PhysRevB.108.165138)

## I. INTRODUCTION

Model Hamiltonians like the Holstein [1], Fröhlich [2], and Su-Schrieffer-Heeger (SSH) [3,4] models have played a central role in formulating our understanding of strong electron-phonon ( $e$ -ph) interactions in solids. These models capture essential aspects of the  $e$ -ph problem while also lending themselves more easily to nonperturbative simulations using powerful numerical methods [5–24]. Auxiliary field quantum Monte Carlo (QMC) methods, for example, can simulate these models without a Fermion sign problem, which allows one to obtain numerically exact results down to low temperatures and across a range of model parameters.

The  $e$ -ph interaction in the Holstein and Fröhlich models arises from a coupling between the lattice displacements and the electron density. This coupling is on-site in the case of the Holstein model and long-range in the Fröhlich model. These models couple the lattice’s motion to the electron’s potential energy. Alternatively, the SSH model couples the lattice displacements to the nearest-neighbor electronic hopping integral  $t$ , thus modulating the electron’s kinetic energy [3,4]. This type of  $e$ -ph interaction was first proposed in a model Hamiltonian context by Barišić, Labbé, and Friedel in 1970 [3] to describe phonon-mediated superconductivity in transition metals, and later by Su, Schrieffer, and Heeger to describe polyacetylene [4]. Nowadays, this microscopic coupling is often referred to as an “SSH” or “Peierls” coupling due to its importance in the Peierls transition in one dimension (1D) [25]. More recently, SSH-like  $e$ -ph interactions have attracted a significant amount of interest [7,24,26–40] due to their potential relevance to high- $T_c$  superconductivity [28,29,33,35] and topological states of matter [38–40].

One can find several variants of the single-band SSH model in the literature (see also Sec. II). The first is the acoustic SSH (aSSH) model as it was initially proposed [3,4], where an acoustic phonon branch modulates the nearest-neighbor hopping integrals to linear order in the relative distance between the atoms. There are also two common optical variants of the model; the first, which we refer to as the “optical” SSH (oSSH) model [7], replaces the acoustic phonons with a dispersionless optical Einstein branch while retaining the acoustic model’s  $e$ -ph interaction terms. The second, which we refer to as the “bond” SSH (bSSH) model [26], defines independent harmonic oscillators for each bond in the system, describing the relative displacement between the atoms forming the bond.

An important distinction among these models is that the displacement of an individual atom simultaneously modulates two neighboring hopping integrals in the acoustic and optical models. In contrast, each hopping integral is modulated independently in the bond model. We will demonstrate that this difference significantly affects how the electrons couple to the  $\mathbf{q} = 0$  modes.

The aSSH model has traditionally been challenging to simulate because its dispersion vanishes as  $\Omega_{\mathbf{q}} \sim v_s |q|$  at the Brillouin zone center, where  $v_s$  is the velocity of sound. QMC methods, for example, face long autocorrelation times when applied to modeling phonon modes with energies  $\Omega_{\mathbf{q}}/t \ll 1$  [41], which has generally prevented simulation of models with low-energy optical and acoustic branches. For this reason, many studies have instead focused on the bond and optical SSH models [27,29–31,34,36,37]. One can also view these models as describing a lattice with a basis where the optical bond-stretching motion of the atoms is naturally expected.

The interactions in the bSSH model have the added advantage of being easier to implement in QMC simulations.

These aspects have led some to focus on the bond SSH model as an effective model for the optical or acoustic versions of the model. This viewpoint is supported by a recent study by Weber *et al.* [27], who examined the equivalency of the aSSH and bSSH models in a 1D chain at half-filling.<sup>1</sup> In that study, the authors obtained effective  $e$ - $e$  interactions by integrating the phonons out of the Hamiltonian and then performed continuous time QMC simulations of the resulting effective model. While this approach allowed them to overcome the autocorrelation time problem associated with the acoustic phonons, it sometimes introduces a Fermion sign problem. Nevertheless, Weber *et al.* [27] were able to compare results for the bond and acoustic models at half-filling and concluded that the models could indeed be mapped onto one another for suitable re-scaling of the  $e$ -ph coupling constant and characteristic phonon energies. However, they did not examine the equivalence of the bond and acoustic models away from half-filling. Nor did they study the optical variant of the SSH model. Therefore, it is an open question whether the three SSH model variants can be regarded as equivalent over more comprehensive ranges of parameter space.

Here we study the (in)equivalence of the acoustic, bond, and optical SSH models in 1D using numerically exact determinant quantum Monte Carlo (DQMC) simulations. To facilitate this study, we employ a hybrid Monte Carlo (HMC) sampling scheme [42–45], which enables simulations of  $e$ -ph coupled models on large clusters and with physically realistic phonon energies [35,46,47]. Using this approach, we perform numerically exact simulations of all three models down to low temperatures without a Fermion sign problem. At half-filling, we find that the aSSH and oSSH models are equivalent for an adequately defined value of the dimensionless coupling and suitably scaled phonon energies. In contrast, the bSSH model produces qualitatively different results, contrary to the conclusions of Ref. [27]. Away from half-filling, we find that all three models are inequivalent; however, the differences between the oSSH and aSSH models remain small while the larger discrepancies with the bSSH model persist. We also find that the total length of the chains shrinks in our simulations of the bSSH model. This behavior is driven by a kinetic energy lowering mechanism, where every bond contracts by some amount to increase the magnitude of the effective hopping integrals, and is unique to this model. We expect our results to hold in higher dimensions and in the presence of electron correlations and thus have implications for future QMC simulations of models involving SSH-like interactions.

## II. METHODS

### A. Classes of single-band SSH models

In this section, we provide definitions for the three variants of the SSH model considered in this paper: the acoustic, bond, and optical SSH models. For the general discussion, we

assume each model is defined on a  $D$ -dimensional hypercubic lattice with one orbital per unit cell and only nearest-neighbor hopping.

The Hamiltonian for all three models can be partitioned as

$$\hat{H} = \hat{H}_e + \hat{H}_{\text{ph}} + \hat{H}_{e\text{-ph}}, \quad (1)$$

where  $\hat{H}_e$  and  $\hat{H}_{\text{ph}}$  describe the noninteracting electronic and lattice degrees of freedom, respectively, and  $\hat{H}_{e\text{-ph}}$  describes their coupling.

In all three cases, the electron degrees of freedom are described using a single-band tight-binding model

$$\hat{H}_e = -t \sum_{\mathbf{i}, \nu, \sigma} (\hat{c}_{\mathbf{i}+\mathbf{a}_\nu, \sigma}^\dagger \hat{c}_{\mathbf{i}, \sigma} + \text{H.c.}) - \mu \sum_{\mathbf{i}, \sigma} \hat{n}_{\mathbf{i}, \sigma}. \quad (2)$$

Here,  $\hat{c}_{\mathbf{i}, \sigma}^\dagger$  ( $\hat{c}_{\mathbf{i}, \sigma}$ ) creates (annihilates) a spin- $\sigma$  ( $=\uparrow, \downarrow$ ) electron at lattice site  $\mathbf{i}$  and  $\hat{n}_{\mathbf{i}, \sigma} = \hat{c}_{\mathbf{i}, \sigma}^\dagger \hat{c}_{\mathbf{i}, \sigma}$  is the spin- $\sigma$  electron number operator for site  $\mathbf{i}$ . The sum over  $\nu$  runs over each of the  $D$  spatial dimensions, with  $\mathbf{a}_\nu$  a lattice vector with corresponding lattice spacing  $a = |\mathbf{a}_\nu|$ . Lastly,  $t$  is the nearest-neighbor hopping integral, and  $\mu$  is the chemical potential.

In the original aSSH model, the neighboring lattice displacements are coupled by a harmonic potential such that

$$\hat{H}_{\text{ph}} = \sum_{\mathbf{i}, \nu} \left( \frac{\hat{P}_{\mathbf{i}, \nu}^2}{2M_a} + \frac{1}{2} K_a (\hat{X}_{\mathbf{i}+\mathbf{a}_\nu, \nu} - \hat{X}_{\mathbf{i}, \nu})^2 \right), \quad (3)$$

where  $\hat{X}_{\mathbf{i}, \nu}$  and  $\hat{P}_{\mathbf{i}, \nu}$  denote the position and momentum operators describing the motion of the atom at site  $\mathbf{i}$  in the direction  $\mathbf{a}_\nu$ .  $K_a$  parameterizes the harmonic potential, and  $M_a$  is the ion mass. The characteristic frequency of the oscillations is then  $\Omega_a = \sqrt{K_a/M_a}$ . The coupling between neighboring sites in Eq. (3) results in  $D$  acoustic phonon branches labeled by  $\nu$ , each corresponding to the motion of the ions polarized along one of the  $D$  spatial directions. The corresponding dispersion relation is acoustic, with a linear dispersion at the zone center.

The linear dispersion of the acoustic model can be difficult to simulate using methods like QMC. To overcome this limitation, the oSSH and bSSH models replace the coupled atomic modes with localized Einstein modes

$$\hat{H}_{\text{ph}} = \sum_{\mathbf{i}, \nu} \left( \frac{\hat{P}_{\mathbf{i}, \nu}^2}{2M_{(o,b)}} + \frac{1}{2} K_{(o,b)} \hat{X}_{\mathbf{i}, \nu}^2 \right), \quad (4)$$

where  $K_o$  ( $M_o$ ) and  $K_b$  ( $M_b$ ) are the spring constant (ion mass) in the oSSH and bSSH models, respectively. The phonon frequency in each case is then given by  $\Omega_{(o,b)} = \sqrt{K_{(o,b)}/M_{(o,b)}}$ . The difference between these models is that the phonons are understood to live on the sites in the oSSH model and the bonds in the bSSH model.

The oSSH and bSSH models share the same form for the lattice degrees of freedom  $\hat{H}_{\text{ph}}$ , while the aSSH and oSSH models share the same form for the  $e$ -ph coupling term  $\hat{H}_{e\text{-ph}}$  in position space. Specifically, the hopping integral is modulated by a term that is linear in the relative distance between neighboring ions

$$\hat{H}_{e\text{-ph}} = \alpha_{(a,o)} \sum_{\mathbf{i}, \nu, \sigma} (\hat{X}_{\mathbf{i}+\mathbf{a}_\nu, \nu} - \hat{X}_{\mathbf{i}, \nu}) (\hat{c}_{\mathbf{i}+\mathbf{a}_\nu, \sigma}^\dagger \hat{c}_{\mathbf{i}, \sigma} + \text{H.c.}). \quad (5)$$

<sup>1</sup>Weber *et al.* [27] use the term ‘‘optical’’ SSH model for what we call the bond SSH model.

Here  $\alpha_a$  and  $\alpha_o$  denote the microscopic  $e$ -ph coupling constant for the aSSH and oSSH models, respectively. In the bSSH model, each phonon mode is instead only associated with a single bond

$$\hat{H}_{e\text{-ph}} = \alpha_b \sum_{i,v,\sigma} \hat{X}_{i,v} (\hat{c}_{i+a_v,\sigma}^\dagger \hat{c}_{i,\sigma} + \text{H.c.}), \quad (6)$$

such that each phonon mode modulates only a single hopping integral.

All three of these models can be expressed in momentum space in the generalized form ( $\hbar = 1$ )

$$\begin{aligned} \hat{H} = & \sum_{\mathbf{k},\sigma} \xi(\mathbf{k}) \hat{c}_{\mathbf{k},\sigma}^\dagger \hat{c}_{\mathbf{k},\sigma} + \sum_{\mathbf{q},\nu} \Omega_\nu(\mathbf{q}) (\hat{b}_{\mathbf{q},\nu}^\dagger \hat{b}_{\mathbf{q},\nu} + \frac{1}{2}) \\ & + \frac{1}{\sqrt{N}} \sum_{\mathbf{k},\mathbf{q},\nu,\sigma} g_\nu(\mathbf{k}, \mathbf{q}) \hat{c}_{\mathbf{k}+\mathbf{q},\sigma}^\dagger \hat{c}_{\mathbf{k},\sigma} (\hat{b}_{-\mathbf{q},\nu}^\dagger + \hat{b}_{\mathbf{q},\nu}), \end{aligned} \quad (7)$$

where  $\xi(\mathbf{k}) = \epsilon(\mathbf{k}) - \mu$  and  $\epsilon(\mathbf{k}) = -2t \sum_\nu \cos(k_\nu a)$  is the bare electron dispersion,  $\Omega_\nu(\mathbf{q})$  is the bare phonon dispersion, and  $g_\nu(\mathbf{k}, \mathbf{q})$  is the  $e$ -ph coupling constant, which depends on both electron momentum  $\mathbf{k}$  and phonon mode momentum  $\mathbf{q}$ .

In the case of the oSSH and bSSH models the bare phonon dispersion is simply  $\Omega_\nu(\mathbf{q}) = \Omega_{(o,b)}$ , whereas in the aSSH model it is

$$\Omega_\nu(\mathbf{q}) = 2\Omega_a \left| \sin\left(\frac{q_\nu a}{2}\right) \right|. \quad (8)$$

Likewise, the specific functional form of  $g_\nu(\mathbf{k}, \mathbf{q})$  depends on the model (acoustic vs optical vs bond). It is convenient to re-express the momentum-dependent  $e$ -ph coupling as

$$g_\nu(\mathbf{k}, \mathbf{q}) = g_\nu \cdot f_\nu(\mathbf{k}, \mathbf{q}), \quad (9)$$

where  $f_\nu(\mathbf{k}, \mathbf{q})$  contains the momentum dependence,

$$g_\nu = \frac{\alpha}{\sqrt{2M\Omega_\nu(\mathbf{q}_{\text{ns}})}} \quad (10)$$

is a constant, and  $\mathbf{q}_{\text{ns}}$  is the best available nesting wavevector for the noninteracting Fermi surface (FS). The momentum-dependent piece for each model is [48,49]

$$\begin{aligned} f_{a,v}(\mathbf{k}, \mathbf{q}) &= 4i \sqrt{\left| \sin\left(\frac{q_\nu a}{2}\right) \right|} \cos((k_\nu + q_\nu/2)a), \\ f_{o,v}(\mathbf{k}, \mathbf{q}) &= 4i \sin\left(\frac{q_\nu a}{2}\right) \cos((k_\nu + q_\nu/2)a), \\ f_{b,v}(\mathbf{k}, \mathbf{q}) &= 2 e^{iq_\nu a/2} \cos((k_\nu + q_\nu/2)a). \end{aligned} \quad (11)$$

One can immediately infer that  $g_\nu(\mathbf{k}, 0) = 0$  for both the aSSH and oSSH models, whereas this is not the case in the bSSH model.

### B. The dimensionless coupling parameter

When simulating models with  $e$ -ph coupling, a key parameter is the dimensionless coupling  $\lambda$ . This parameter, for example, enters into the superconducting  $T_c$  of a conventional superconductor when treated at the level of BCS or Eliashberg theory [50,51]. For a momentum-dependent  $e$ -ph coupling

constant  $g(\mathbf{k}, \mathbf{q})$ ,  $\lambda$  is defined as

$$\begin{aligned} \lambda &= 2\mathcal{N}(0) \sum_\nu \left\langle \left\langle \frac{|g_\nu(\mathbf{k}, \mathbf{q})|^2}{\Omega_\nu(\mathbf{q})} \right\rangle \right\rangle_{\text{FS}} \\ &= 2\mathcal{N}(0) \sum_\nu \left( \frac{\frac{1}{N^2} \sum_{\mathbf{k},\mathbf{q}} \frac{|g_\nu(\mathbf{k}, \mathbf{q})|^2}{\Omega_\nu(\mathbf{q})} \delta(\xi(\mathbf{k} + \mathbf{q})) \delta(\xi(\mathbf{k}))}{\frac{1}{N^2} \sum_{\mathbf{k},\mathbf{q}} \delta(\xi(\mathbf{k} + \mathbf{q})) \delta(\xi(\mathbf{k}))} \right) \\ &= \frac{2}{\mathcal{N}(0)N^2} \sum_{\mathbf{k},\mathbf{q},\nu} \frac{|g_\nu(\mathbf{k}, \mathbf{q})|^2}{\Omega_\nu(\mathbf{q})} \delta(\xi(\mathbf{k} + \mathbf{q})) \delta(\xi(\mathbf{k})), \end{aligned} \quad (12)$$

where  $\mathcal{N}(0) = \frac{1}{N} \sum_{\mathbf{k}} \delta(\xi(\mathbf{k}))$  is the density of states at the FS per spin species and  $\langle \langle \cdot \rangle \rangle_{\text{FS}}$  denotes a FS average. We will denote  $\lambda$  defined in this way as  $\lambda^{\text{FS}}$ .

We now consider two simple schemes for approximating  $\lambda^{\text{FS}}$ . In both approximations, we assume a constant density of states and set  $\mathcal{N}(0) \approx W^{-1}$ , with  $W = 4Dt$  the noninteracting bandwidth. In the first scheme, we additionally remove the  $\delta$ -functions appearing in Eq. (12) and perform a simple average over the Brillouin zone such that

$$\lambda^{\text{BZ}} = \frac{2}{WN^2} \sum_{\mathbf{k},\mathbf{q},\nu} \frac{|g_\nu(\mathbf{k}, \mathbf{q})|^2}{\Omega_\nu(\mathbf{q})}. \quad (13)$$

In the second scheme, we approximate  $\lambda^{\text{FS}}$  by

$$\begin{aligned} \lambda^{\text{const}} &= \frac{2}{W} \sum_\nu \frac{\max(|g_\nu(\mathbf{k}, \mathbf{q}_{\text{ns}})|^2)}{\Omega_\nu(\mathbf{q}_{\text{ns}})} \\ &= \frac{2}{W} \sum_\nu \frac{g_\nu^2}{\Omega_\nu(\mathbf{q}_{\text{ns}})} \max(|f_\nu(\mathbf{k}, \mathbf{q}_{\text{ns}})|^2), \end{aligned} \quad (14)$$

where  $\max(\cdot)$  indicates the maximum of  $|f_\nu(\mathbf{k}, \mathbf{q}_{\text{ns}})|^2$  as a function of  $\mathbf{k}$ .

We will show that at half-filling ( $\mu = 0$ ), the aSSH and oSSH are approximately equivalent when  $\lambda_a^{\text{const}} = \lambda_o^{\text{const}} = \lambda_b^{\text{const}}$  and  $2\Omega_a = \Omega_o = \Omega_b$  for small dimensionless couplings, while the bSSH model is inequivalent to the other two. The second condition arises from requiring  $\Omega(\mathbf{q}_{\text{ns}})$  to be the same for all three models.

### C. Expressions for a 1D model

The discussion until this point applies to single-band SSH models defined on  $D$ -dimensional hypercubic lattices. To test the equivalence of the three models using DQMC, we focus on 1D chains with nearest-neighbor hopping. In 1D, we fix  $|\mathbf{q}_{\text{ns}}| = \pi/a$ , the nesting wavevector at half-filling, even as we dope the system. Applying this definition to each of the three models results in  $g_a = \alpha_a/\sqrt{4M_a\Omega_a}$ ,  $g_o = \alpha_o/\sqrt{2M_o\Omega_o}$ , and  $g_b = \alpha_b/\sqrt{2M_b\Omega_b}$  for the aSSH, oSSH, and bSSH models, respectively.

Using the appropriate functional forms for  $e$ -ph coupling, the Brillouin-zone average approximation introduced in

Eq. (13) results in

$$\begin{aligned}\lambda_a^{\text{BZ}} &= \frac{2\alpha_a^2}{M_a\Omega_a^2W}, \\ \lambda_o^{\text{BZ}} &= \frac{4\alpha_o^2}{M_o\Omega_o^2W}, \\ \lambda_b^{\text{BZ}} &= \frac{2\alpha_b^2}{M_b\Omega_b^2W},\end{aligned}\quad (15)$$

for the aSSH, oSSH, and bSSH models, respectively. Alternatively, the approximation introduced in Eq. (14) results in

$$\begin{aligned}\lambda_a^{\text{const}} &= \frac{4\alpha_a^2}{M_a\Omega_a^2W}, \\ \lambda_o^{\text{const}} &= \frac{16\alpha_o^2}{M_o\Omega_o^2W}, \\ \lambda_b^{\text{const}} &= \frac{4\alpha_b^2}{M_b\Omega_b^2W},\end{aligned}\quad (16)$$

for each model. We will show that this second approximation results in an approximate equivalence between the aSSH and oSSH models at half-filling.

Finally, when computing  $\lambda^{\text{FS}}$  given by Eq. (12), we approximate the  $\delta$  functions using Lorentzian distributions with a full-width at half-maximum of  $\Gamma = 0.01t$  and perform the corresponding momentum sums using  $10^3$   $k$ -points in the first Brillouin zone.

#### D. Quantum Monte Carlo

We studied Eq. (1) using sign-problem free DQMC simulations [52] on 1D chains of length  $L$  with periodic boundary conditions. Our implementation uses the HMC method to sample the phonon fields while adopting both Fourier acceleration and time-step splitting to help reduce autocorrelation times [42,43,45]. The HMC updates use forces calculated by evaluating the exact derivative of the total action as it appears in the Monte Carlo weights used in DQMC [53]. The simulations, therefore, have a computational cost that scales as  $O(\beta L^3)$  in 1D. Finally, when simulating the acoustic model, we subtract off the center of mass motion of the lattice  $X_{\text{cm}} \equiv \sum_{i,l} X_i(\tau = l\Delta\tau)$  after every HMC update. However, in practice, we have found that this subtraction does not affect any measured quantities other than  $\langle X \rangle$  itself.

All simulations were performed with 12 or 24 parallel Markov chains, each performing  $10^4$  warm-up sweeps and  $2.5 \times 10^4$  measurement sweeps, with 1250 measurements per bin for a total of 20 measurements of each observable per Markov chain. In all cases, the imaginary time discretization was set to  $\Delta\tau t = 1/20$ .

In DQMC simulations, it is possible to measure the expectation value of a wide variety of correlation functions.

To detect bond-ordered wave (BOW) correlations, we measure the real-space bond correlation function

$$S_B(r, \tau) = \frac{1}{L} \sum_i \langle \hat{B}_{i+r}(\tau) \hat{B}_i(0) \rangle, \quad (17)$$

where

$$\hat{B}_i = \sum_{\sigma} (\hat{c}_{i+1,\sigma}^{\dagger} \hat{c}_{i,\sigma} + \text{H.c.}) \quad (18)$$

is the nearest-neighbor bond operator. The bond structure factor is then obtained by a Fourier transform

$$S_B(q, \tau) = \sum_r e^{-iqr} S_B(r, \tau), \quad (19)$$

while the corresponding bond susceptibility is

$$\chi_B(q) = \int_0^{\beta} S(q, \tau) d\tau. \quad (20)$$

By performing analytic continuation on the electron Green's function using a parameter-free differential evolution algorithm for analytic continuation (DEAC) [54], we reconstruct the electron spectral function. For the electrons, they are related by

$$G_{\sigma}(k, \tau) = \int_0^{\beta} d\omega \frac{e^{-\tau\omega}}{1 + e^{-\beta\omega}} A(k, \omega). \quad (21)$$

In the case of phonons, we measure the phonon position correlation function in momentum space

$$C_X(q, \tau) = \frac{1}{L} \sum_{i,r} e^{-iqr} \langle \hat{X}_{i+r}(\tau) \hat{X}_i(0) \rangle, \quad (22)$$

which is related to the standard phonon Green's function  $D(q, \tau)$  according to

$$D(q, \tau) + D(q, \beta - \tau) = 2M\Omega(q)C_X(q, \tau). \quad (23)$$

We then use the phonon Green's function to extract the renormalized phonon energy

$$\Omega(q, 0) = \sqrt{\Omega^2(q) + \Pi(q, 0)}, \quad (24)$$

where  $\Pi(q, i\nu_n)$  is a function related to the phonon self-energy and  $\nu_n = 2\pi n/\beta$  is bosonic Matsubara frequency. This function is related to the phonon Green's function according to

$$D(q, i\nu_n) = \frac{2\Omega(q)}{(i\nu_n)^2 - \Omega^2(q) - \Pi(q, i\nu_n)}. \quad (25)$$

### III. RESULTS

We will present DQMC results for the models in 1D in this section. However, some preliminary comments are in order before proceeding. First, we focus on the weak-coupling limit throughout most of this section to avoid complications arising from potential sign changes in the effective hopping integrals. This issue stems from the linear approximation for the  $e$ -ph interaction, which allows the effective distance-dependent hopping to have an unphysical sign change whenever the lattice displacements become sufficiently large [30,31]. Appendix A discusses this issue in greater detail and examines the differences in how the three models approach this limit.

Second, we will largely focus on results obtained from  $L = 24$  site chains throughout this section, even though we have observed some finite-size effects (see Appendix B). (We will present some results for longer  $L = 64$  site chains when we examine the spectral functions and renormalized phonon dispersion relations in Secs. III D and III E.) These



TABLE I. The microscopic values of the  $e$ -ph coupling needed to fix the value of the dimensionless coupling to 0.2 using the indicated approximations, with  $2\Omega_a = \Omega_o = \Omega_b = 0.1$ . The quantity  $\lambda_{k_F, 2k_F} \equiv |g(k_F, 2k_F)|^2 / \Omega(2k_F)$  denotes the value of the momentum dependent coupling constant for scattering with  $k_F = \pi/2$  and  $2k_F = \pi$ .

Quantity	Fixed $\lambda^{\text{FS}}$	Fixed $\lambda^{\text{BZ}}$	Fixed $\lambda^{\text{const}}$
$\alpha_a$	0.0394	0.0316	0.0224
$\alpha_o$	0.0395	0.0447	0.0224
$\alpha_b$	0.0787	0.0632	0.0447
$\lambda_{k_F, 2k_F}^a$	1.2398	0.8000	0.4000
$\lambda_{k_F, 2k_F}^o$	1.2459	1.6000	0.4000
$\lambda_{k_F, 2k_F}^b$	1.2398	0.8000	0.4000

include an oscillation in the  $q = \pi$  bond correlations at half-filling, where the strength of the correlations is under-(over-)predicted relative to the thermodynamic limit for  $L = 4n$  ( $2n$ ), where  $n$  is an integer. In other words, the bond correlations' strength appears to approach the thermodynamic limit from above or below, depending on whether or not the chain contains an odd number of doubled unit cells associated with the bond-ordered phase. Nevertheless, we have found that the lattice's finite size only affects the quantitative results and not the (in)equivalence of the three SSH models (provided that a consistent chain length is used when making comparisons). Therefore, we will proceed with  $L = 24$  site chains, which are rather inexpensive to simulate down to low temperatures.

### A. Filling vs chemical potential

Figure 1 plots  $\langle n \rangle$  vs  $\mu$  for all three models, where we have fixed the dimensionless coupling  $\lambda = 0.2$  using the indicated approximation scheme. For reference, Table I provides the corresponding values of the microscopic  $e$ -ph coupling constants, showing how they differ in each approximation for  $\lambda$ .

For fixed  $\lambda^{\text{const}} = 0.2$  [see Fig. 1(a)],  $\langle n \rangle$  is a smooth function of  $\mu$  for all three models with no clear indications of an energy gap at  $\beta = 15/t$ . The behavior of the aSSH and oSSH models are identical to within the simulation's error bars for this approximation for the dimensionless coupling. Moreover, the bandwidth inferred from these curves remains equal to the noninteracting value  $W = 4t$ . On the other hand, the behavior of  $\langle n \rangle$  vs  $\mu$  for the bSSH model differs from the acoustic and optical models with an apparent bandwidth increase. This behavior is also seen in the single-particle spectral functions discussed in Sec. III D.

Constraining the value of  $\lambda^{\text{BZ}} = 0.2$  [see Fig. 1(b)] leads to deviations in the  $\langle n \rangle$  vs  $\mu$  curves of all three models. The most significant difference between the acoustic and optical models occurs close to half-filling due to the formation of a robust  $q = \pi$  bond ordering in the oSSH model (see Sec. III C). The difference between the bSSH model and both the oSSH and aSSH models also become more pronounced, with the bandwidth of the bond model increasing relative to the results shown in Fig. 1(a). Fixing  $\lambda^{\text{FS}} = 0.2$  [see Fig. 1(c)] results in even more significant deviations between the three models. For this coupling, all three models have a gap associated with the bond order, with the oSSH (bSSH) model having the largest (smallest) gap. Constraining  $\lambda^{\text{FS}} = 0.2$  also further

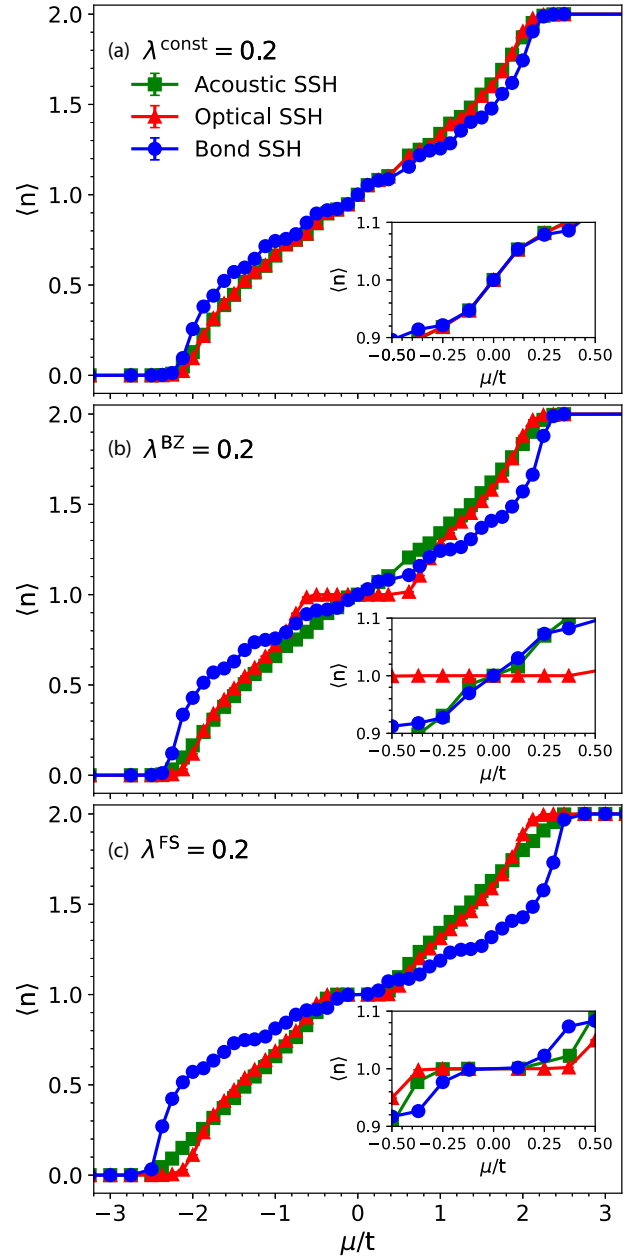


FIG. 1. The total filling  $\langle n \rangle$  as a function of chemical potential  $\mu$  for the acoustic (green  $\square$ ), bond (blue  $\circ$ ), and optical (red  $\triangle$ ) SSH models with fixed (a)  $\lambda^{\text{const}} = 0.2$ , (b)  $\lambda^{\text{BZ}} = 0.2$ , and (c)  $\lambda^{\text{FS}} = 0.2$ . All three panels show results obtained on an  $L = 24$  site chain with  $\Omega_b = \Omega_o = 2\Omega_a = 0.1$  and  $\beta = 15/t$ .

increases the effective bandwidth for the bSSH model, while the other models acquire some widening due to the self-energy broadening of the electronic structure.

The increasing deviations between the models for the BZ- and FS-averaged values of  $\lambda$  stem from differences in how these approximations average the momentum dependence of the coupling constants  $g(k, q)$ . For weak  $e$ -ph coupling, the physics of the models is dominated by scattering processes across the Fermi surface, i.e.,  $k_F = \pi/2$  and  $q = 2k_F = \pi$  at half-filling. Fixing  $\lambda^{\text{const}}$  for the 1D model imposes the condition that the mode-resolved dimensionless coupling

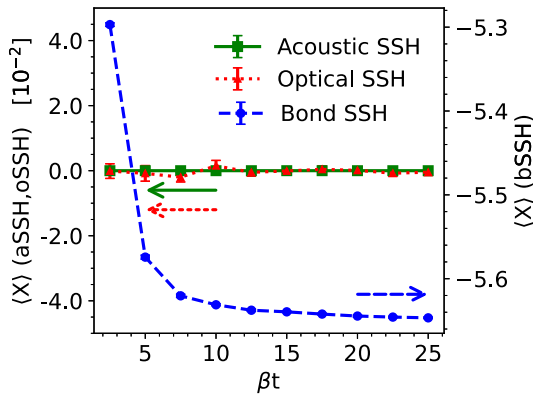


FIG. 2. The expectation value of the average phonon displacement  $\langle X \rangle$ , with a corresponding net change in the length of the lattice  $\Delta L = L\langle X \rangle$ . Results were obtained here for a half-filled ( $\mu = 0$ )  $L = 24$  chain with  $\lambda^{\text{const}} = 0.2$  and  $\Omega_b = \Omega_o = 2\Omega_a = 0.1$ . The  $y$  axis on the left-hand side of the plot is for the acoustic (green  $\square$ ) and optical (red  $\triangle$ ) SSH models. The  $y$  axis on the right-hand side of the plot is for the bond SSH model (blue  $\circ$ ).

$\lambda_{k_F, 2k_F} \equiv |g(k_F, 2k_F)|^2 / \Omega(2k_F)$  be the same for all three models. Conversely, fixing  $\lambda^{\text{BZ}}$  or  $\lambda^{\text{FS}}$ , which involves different averages of the momentum-dependent coupling  $|g(k, q)|^2$ , translates into different values for this quantity, as summarized in Table I. This rescaling of the effective scattering across the FS also explains the different values of the relative gap sizes inferred in Fig. 1.

These considerations imply that one should fix  $\lambda^{\text{const}}$  if one wishes to make direct comparisons between the different SSH models in 1D. We do not, however, expect this to generally be the case in higher dimensions if the Fermi surface is not perfectly nested; in that case, one should use either BZ- or FS-averaged dimensionless couplings to correctly average over the different scattering processes that enter when the relevant Fermi surfaces are no longer perfectly nested.

### B. Contraction of the lattice in the bond model

As noted in the Introduction, the bSSH model differs from the acoustic and optical models in how it couples to the  $q = 0$  phonon modes. In the acoustic and optical models, the displacement of individual atoms simultaneously shortens one of its neighboring bonds and lengthens the other. This constraint maintains the total length of the chain at all times and decouples the electrons from the  $\mathbf{q} = 0$  phonon mode, which is the reason why  $\lim_{q \rightarrow 0} g_{o,a}(k, q) \rightarrow 0$  [see Eq. (11)]. We can easily understand this behavior by recognizing that a  $q = 0$  mode in the acoustic or optical models translates the chain to the left or right without changing internal bond lengths. The situation is fundamentally different in the bond model. There, the electrons can lower their total kinetic energy by contracting all bonds by the same amount, increasing the effective hopping integrals along each bond. Because of this,  $\lim_{q \rightarrow 0} g_b(k, q) \neq 0$  for the bond model [see Eq. (11)], and the total length of the chain is no longer conserved.

Figure 2 confirms these expectations by plotting the net change in the length of the chain  $\Delta L/L$  for all three models as a function of temperature when  $\langle n \rangle = 1$  and  $\lambda^{\text{const}} = 0.2$ .

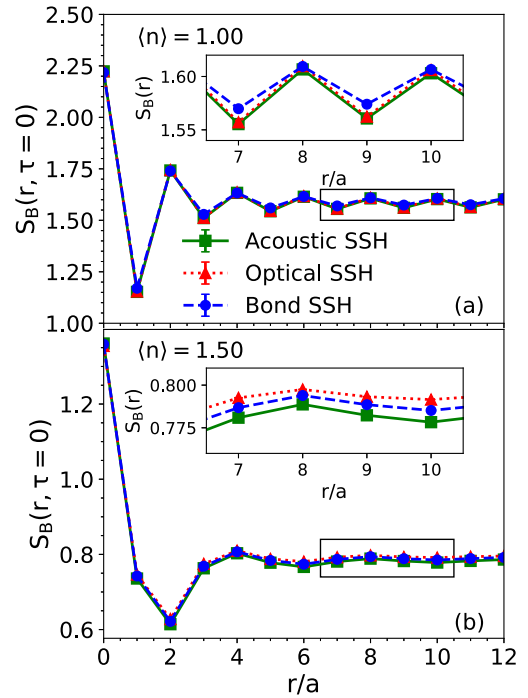


FIG. 3. The real space bond-order correlations  $S_B(r)$  as a function of distance along the chain. Results are shown for (a) half-filling  $\langle n \rangle = 1$  and (b)  $\langle n \rangle = 1.5$  and were obtained on an  $L = 24$  site chain with,  $\lambda^{\text{const}} = 0.2$ ,  $\Omega_b = \Omega_o = 2\Omega_a = 0.1$ , and  $\beta = 15/t$ . The insets in both panels provide a zoomed-in view of the region indicated by the small black boxes in the main panels.

$\Delta L$  is obtained here by averaging the lattice displacements over imaginary time  $\Delta L/L \equiv \frac{1}{N_\tau L} \sum_{i,l} X_i(l\Delta\tau)$ , where  $l = 0, \dots, N_\tau$  and  $N_\tau$  is the number of imaginary time slices. As expected,  $\Delta L$  fluctuates around zero within error bars for the acoustic and optical SSH models at all temperatures. Conversely, it drops from  $\Delta L/L = -5.297 \pm 0.002$  at  $\beta = 2.5/t$  to  $-5.647 \pm 0.001$  at  $\beta = 25/t$  for the bond model as the thermal fluctuations of the lattice freeze out. Notably, this effect is not limited to 1D as we have also observed it in simulations of the bond model in 2D whenever there is a nonzero  $e$ -ph coupling.

### C. Bond-order correlations

It is well known that the half-filled 1D SSH models are prone to lattice dimerization at low temperatures. This transition, often referred to as the Peierls transition [25], is accompanied by  $q = \pi$  bond-order correlations.

Figure 3(a) plots the real-space bond correlations obtained for the three models at half-filling with  $\beta = 15/t$ ,  $\lambda^{\text{const}} = 0.2$ , and  $\Omega_b = \Omega_o = 2\Omega_a = 0.1$ . For these parameters, all three models develop strong  $q = \pi$  correlations that extend along the entire length of the chain. Moreover, the observed correlations for the acoustic and optical models are identical within the error bars. This result further establishes the equivalence of these models after we appropriately fix  $\lambda^{\text{const}}$  and phonon energy scales. The bSSH model also develops comparable bond-order correlations at this temperature, but the overall strength of the modulations is slightly smaller as shown in the

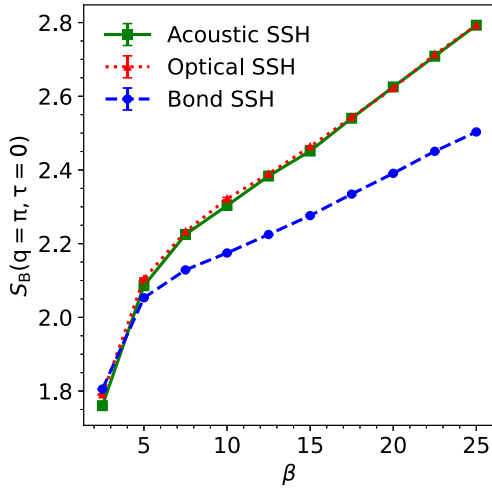


FIG. 4. A comparison of the  $q = \pi$  bond correlations measured in the acoustic (green  $\square$ ), bond (blue  $\circ$ ), and optical (red  $\triangle$ ) SSH models. Results were obtained  $L = 24$  site chain at half-filling  $\langle n \rangle = 1$  ( $\mu = 0$ ) with  $\Omega_b = \Omega_o = 2\Omega_a = 0.1$  and  $\lambda^{\text{const}} = 0.2$  for all three models.

inset. Interestingly, the values of the bond model's correlations on the even distances are comparable to those obtained using the other two models. In contrast, the values at odd distances are slightly larger for the bond model, resulting in a weaker amplitude in the overall modulation.

For comparison, Fig. 3(b) plots the real-space bond correlations for the doped model. In this case, we fix the filling for all three models to  $\langle n \rangle = 1.50$  by tuning the chemical potential during the DQMC simulation as described in Ref. [55]. In all three cases, we observe a bond-order correlation with a wavevector  $q = 2k_F = \pi/2$ , where  $k_F = 3\pi/4$  is the Fermi momentum for the doped system. The strength of the modulations is different for each model because the value of  $\lambda^{\text{const}}$  was fixed based on the Fermi surface of the half-filled system. This result demonstrates that any equivalence achieved between the aSSH and oSSH models at half-filling will not persist once the system is doped unless further changes to the model parameters are made.

Next, Fig. 4 examines how the  $S_B(q = \pi)$  bond correlations observed at half-filling evolve with temperature. At very high temperatures, the system is dominated by thermal fluctuations. The details of the microscopic  $e$ -ph interaction matter very little at this temperature, and the bond correlations' strength is comparable across all three models. As  $T$  decreases, the strength of the bond correlations grows, as expected. The value of  $\chi_B(\pi)$  in the acoustic and optical models is identical within error bars as a function of  $T$ , while the correlations in the bond model are consistently weaker. We can conclude from this data that the equivalency of the oSSH and aSSH models persists across all simulated temperatures and that these models produce stronger bond-correlations compared to the bSSH model for a fixed  $\lambda^{\text{const}}$ .

Figure 5 provides an additional comparison of the imaginary time dependence of the local Green's function  $G(r = 0, \tau)$  [Fig. 5(a)] and bond correlations  $S_B(q = \pi, \tau)$  [Fig. 5(b)]. Again, the acoustic and optical SSH models

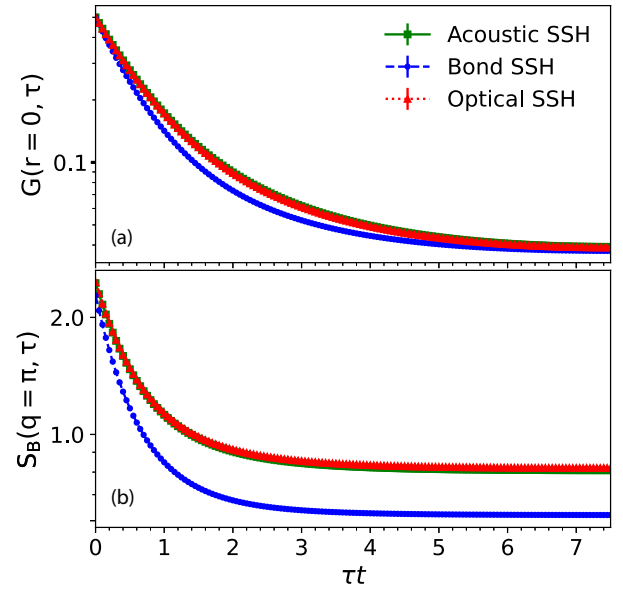


FIG. 5. A comparison of the (a) local Green's function  $G(r = 0, \tau)$  and (b) bond correlations  $S_B(q = \pi, \tau)$  of the acoustic (green  $\square$ ), bond (blue  $\circ$ ), and optical (red  $\triangle$ ) SSH models. Results were obtained  $L = 24$  site chain at half-filling  $\langle n \rangle = 1$  ( $\mu = 0$ ) with  $\Omega_b = \Omega_o = 2\Omega_a = 0.1$ ,  $\beta = 15/t$ , and  $\lambda^{\text{const}} = 0.2$  for all three models. The y-axis is on a long scale in both panels.

produce identical results within error bars for both quantities, while the bond model has quantitatively different results.

#### D. Single-particle spectral functions

We now turn to the spectral properties of the three models in both the weak and strong-coupling limits. Figure 6 plots the single-particle spectral function  $A(k, \omega)$  for the models for fixed  $\lambda^{\text{const}} = 0.2$  (top row) and  $\lambda^{\text{const}} = 0.7$  (bottom row). We have performed the calculations on long  $L = 64$  site chains to achieve fine momentum resolution, and fixed the inverse temperature to  $\beta = 15/t$ .

At weak coupling [Figs. 6(a)–6(c)], all three models produce spectra that disperse through the Fermi level, indicative of a metallic phase at this temperature. All three spectra exhibit canonical signatures of the  $e$ -ph interaction. Specifically, the peaks broaden as the quasiparticle dispersion crosses the phonon energy  $\omega = \pm\Omega(q = \pi)$ , which is a common characteristic of  $e$ -ph coupled systems. This broadening would usually be accompanied by a kink in the band dispersion at  $\omega = \Omega(\pi)$  [56,57], but we are unable to resolve such a feature in our data. This may be due to the low values of the coupling and phonon energy [ $\Omega(\pi)/t = 0.1$ ] or difficulties in resolving such a subtle spectral feature in the analytically continued data. Notably, the spectra for the aSSH and oSSH models are indistinguishable, consistent with the equivalence described in the previous sections, while the bSSH model [Fig. 6(c)] has increased bandwidth  $W \approx 4.6t$ . This latter observation is consistent with the effective bandwidth  $W_{\text{eff}} = 4t_{\text{eff}} = 5t$  one would estimate using a mean-field-like analysis of the effective hopping  $t_{\text{eff}} = t - \alpha_b \langle X \rangle \approx 1.253$  ( $\alpha_b = 0.0447$  and  $\langle X \rangle = -5.666$ , see Fig. 2 and Table I).

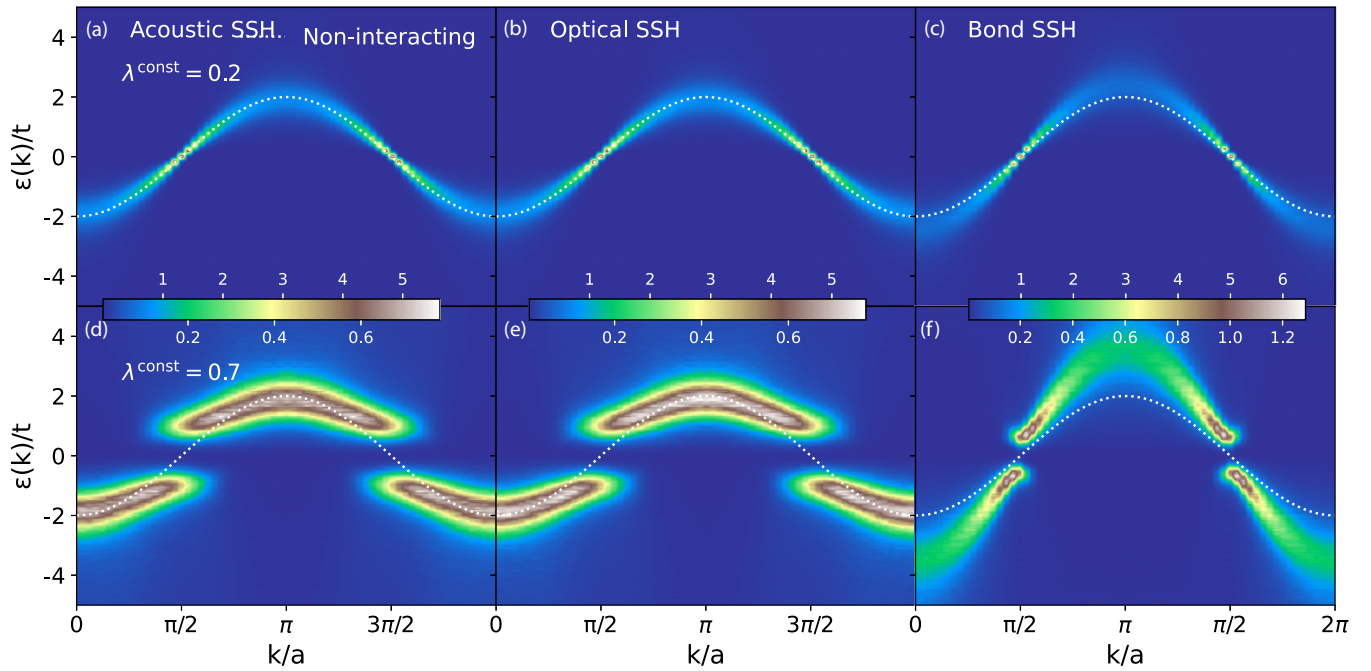


FIG. 6. The single-particle spectral function  $A(k, \omega)$  for the various SSH models. The top row shows results for the (a) acoustic, (b) optical, and (c) bond SSH models with  $\lambda^{\text{const}} = 0.2$ . The bottom row shows results for the same models but this time with  $\lambda^{\text{const}} = 0.7$ . The results in each panel were obtained on  $L = 64$  site chains at half-filling ( $n = 1$  ( $\mu = 0$ )) with  $\Omega_b = \Omega_o = 2\Omega_a = 0.1$  and  $\beta = 15/t$ . The white dashed lines in each panel indicate the noninteracting dispersion at half-filling  $\epsilon(k) = -2t \cos(ka)$ .

Turning now to  $\lambda^{\text{const}} = 0.7$  [Figs. 6(d) and 6(e)], we find that all three spectra are significantly broadened and open a gap at the Fermi level, indicative of bond-order wave (BOW) insulating state. As with the weak-coupling case, the spectra for the aSSH and oSSH models are identical and have a bandwidth comparable to the noninteracting value. Conversely, the bSSH model's spectra are sharper (note the difference in the intensity scale) and have a smaller gap, indicating that the BOW correlations and quasi-particle dressing of the carriers are weaker in the bond model compared to the other two. The observed bandwidth of the bSSH model increases to  $W \approx 7.3t$  for this value of the coupling, which is again consistent with the estimate  $W_{\text{eff}} = 4t_{\text{eff}} = 7.45t$  ( $\langle X \rangle = -10.335$  and  $\alpha_b = 0.0836$ ) obtained from a mean-field-like analysis.

We will discuss the renormalized phonon dispersions for the weak coupling case shortly [see Fig. 7]. However, before we turn to that, Fig. 8 reports strong coupling  $\lambda^{\text{const}} = 0.7$  results for systems doped to quarter filling ( $n = 0.5$ ). Looking at  $A(k, \omega)$  for the aSSH in Fig. 8(a), we see that a gap has opened at  $k = \frac{\pi}{4}$ , with a corresponding nesting wavevector  $q = \frac{\pi}{2}$ , instead of  $q = \pi$  as at half-filling. However, for oSSH model, shown in Fig. 8(b), there is no clearly resolved gap, and the approximate equivalence between the aSSH and oSSH models observed at half-filling has clearly broken down. This result makes sense given that the microscopic  $e$ -ph coupling constant  $\alpha$  was held fixed as each system was doped away from half-filling. Equation (11) indicates that  $f_o(k, q)$  decays to zero more rapidly than  $f_a(k, q)$  as  $q$  shifts from the Brillouin zone edge to the center. Additionally, the bare phonon dispersion at  $\Omega(\pi/4)$  is significantly smaller in the aSSH as compared to the oSSH model, meaning that we expect  $\lambda$ , as defined in

Eq. (12), to be further enhanced in the aSSH model relative to the oSSH model. Finally, the spectra for the bSSH model, shown in Fig. 8(c) has a small gap at quarter-filling. Similar to the half-filled case, the bSSH bandwidth has significantly increased, with the gap falling entirely outside the bandwidth of the corresponding noninteracting dispersion, shown as a dashed white line.

### E. Renormalized phonon dispersions

Figure 7 plots the renormalized phonon dispersion relations  $\Omega(q, iv_n = 0)$  [see Eq. (24)] for the same parameters used in the previous section for half-filling. At weak coupling ( $\lambda^{\text{const}} = 0.2$ ), the dispersion relations are weakly renormalized, with the degree of mode softening increasing as  $q$  approaches the Brillouin zone boundary. The observed softening reflects the formation of BOW correlations driven by FS nesting and the underlying momentum dependence of the  $e$ -ph coupling, which is strongest near the zone boundary [see Eq. (11)]. However, the  $q = \pi$  mode not softening to zero at this temperature is consistent with the absence of a gap in the corresponding single-particle electron spectral function.

Similar  $q$ -dependent normalizations are observed for strong coupling ( $\lambda^{\text{const}} = 0.7$ ); however, the broad dip around the zone boundary becomes shallower in the optical model compared to the weak coupling result. At the same time, a sharp discontinuity appears at  $q = \pi$ , where this mode softens nearly to zero. For this value of the coupling, the system is in an insulating, dimerized state with large lattice displacements. We attribute the finite value of  $\Omega(\pi, 0)$  to a finite-size effect [35]. Interestingly, for both weak and strong coupling we



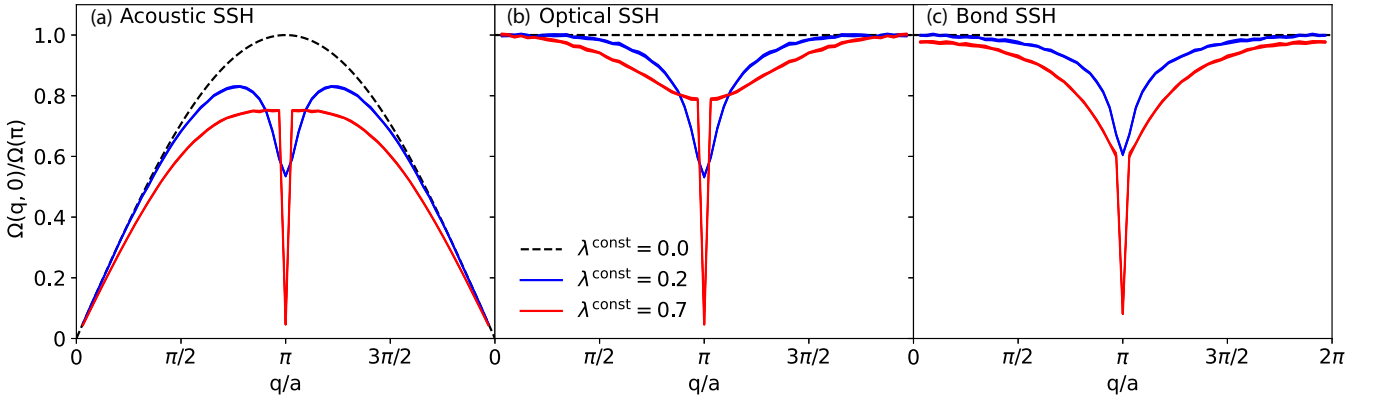


FIG. 7. The renormalized phonon dispersion [see Eq. (24)] for the (a) acoustic, (b) optical, and (c) bond SSH models with  $\lambda^{\text{const}} = 0, 0.2,$  and  $0.7$ . All results were obtained on  $L = 64$  site chains at half-filling ( $n = 1$  ( $\mu = 0$ )) with  $\Omega_b = \Omega_o = 2\Omega_a = 0.1$  and  $\beta = 15/t$ .

find that  $\Omega_a(\pi, 0) = \Omega_o(\pi, 0) \neq \Omega_b(\pi, 0)$ . In addition, the renormalized dispersion for the bSSH model also does not approach its noninteracting value at  $q \rightarrow 0$ , which reflects the fact that this model has a nonzero coupling to this mode. These behaviors are fully consistent with the (in)equivalences between the respective models discussed in the previous sections.

We also remark that we recover the expected linear dispersion for the aSSH model as  $q \rightarrow 0$ , which demonstrates

that our HMC sampling algorithm correctly captures the long-wavelength behavior of this phonon branch.

Next we look at the renormalized phonon dispersion  $\Omega(q, 0)$  in the strong coupling  $\lambda^{\text{const}} = 0.7$  at quarter-filling ( $n = 0.5$ ). The bottom row of Fig. 8 plots the renormalized dispersions for in all three models, where we observe a softening of  $\Omega(q, 0)$  at  $q \approx \frac{\pi}{2}$ . However, rather than the sharp discontinuity at  $q = \pi$  observed in the half-filled strong coupling case, we observe a broader dip similar to the softening

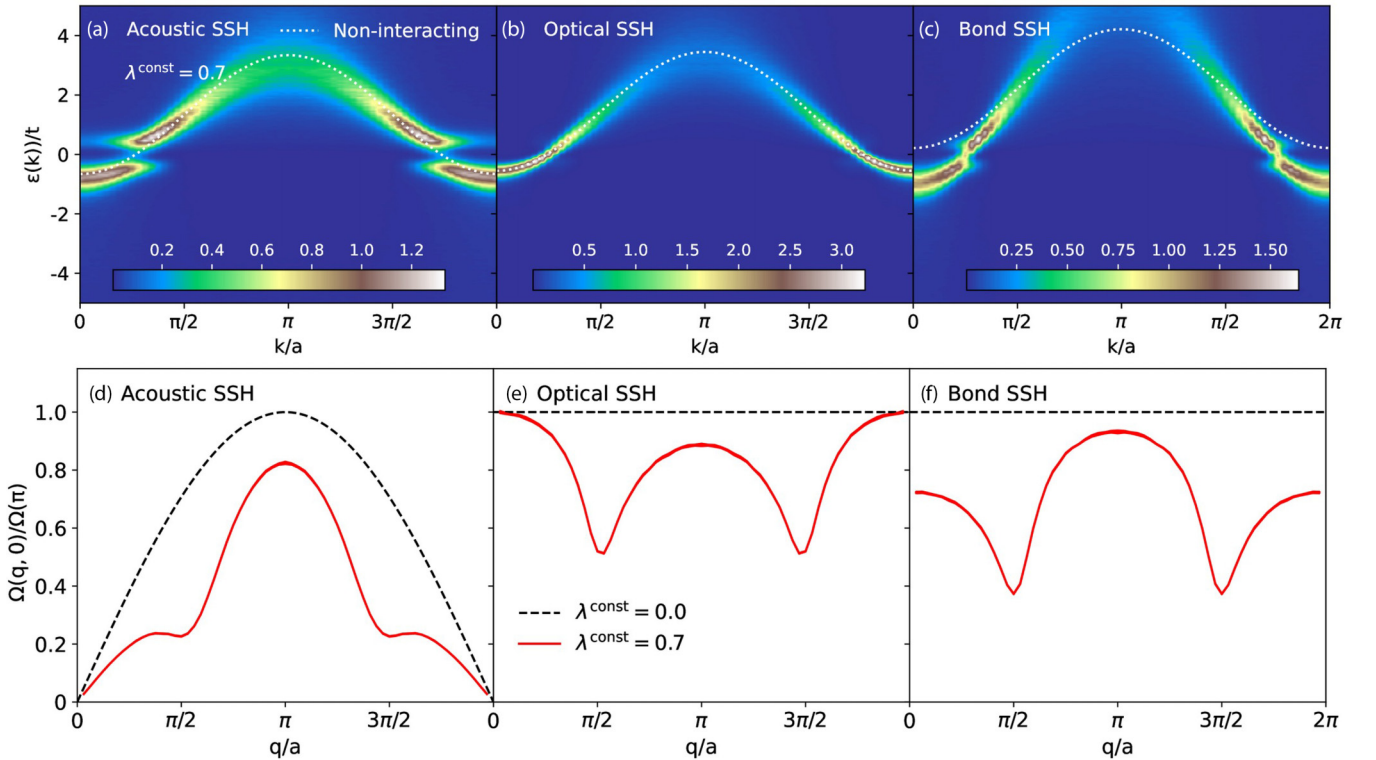


FIG. 8. The single-particle spectral function  $A(k, \omega)$  and renormalized phonon dispersion at quarter-filling ( $n = 0.5$ ). The results in each panel were obtained on  $L = 64$  site chains with  $\lambda^{\text{const}} = 0.7$ ,  $\Omega_b = \Omega_o = 2\Omega_a = 0.1$ , and  $\beta = 15/t$ . In the first row, panels [(a)–(c)], show  $A(k, \omega)$  for the acoustic, optical, and bond SSH models, respectively. The white dashed lines in each of these panels indicate the shifted noninteracting dispersion  $\xi(k) = \epsilon(k) - \mu$ , where the value of the chemical potential  $\mu$  corresponds to the value needed to obtain a density of ( $n = 0.5$ ) in simulations of the interacting system. In the second row, panels [(d)–(f)], show the renormalized phonon dispersion  $\Omega(q, 0)$  for the acoustic, optical, and bond SSH models, respectively.

observed in the half-filled weak-coupling  $\lambda^{\text{const}} = 0.2$  case. This difference results from the true effective dimensionless  $e$ -ph coupling  $\lambda$  in each model decreasing as the system is doped away from half-filling while holding  $\alpha$  fixed.

In the case of the aSSH model, it is interesting that  $A(k, \omega)$  is gapped in Fig. 8(a), but  $\Omega(\pi/2, 0)$  has not softened all the way to zero in Fig. 8(d). This behavior may stem from longer wavelength  $q \approx \frac{\pi}{2}$  bond correlations that more easily gap the spectrum on a finite lattice. Lastly, looking at Fig. 8(f), we see that  $\Omega(q = 0, 0)$  in the bSSH model has been renormalized to a significantly smaller value, again a reflection of the fact that  $g_b(q, k)$  does not go to zero at  $q = 0$ .

#### IV. DISCUSSION

Our results demonstrate that at half-filling, the 1D acoustic and optical SSH models can be made to produce identical results within error bars for a suitable choice of phonon energies and  $e$ -ph coupling constant. One has to set the phonon energy scale and microscopic  $e$ -ph coupling constants such that energy of the  $q = 2k_F = \pi$  modes and mode-resolved dimensionless coupling for scattering across the Fermi surface  $|g(k_F, 2k_F)|^2/\Omega(2k_F)$  are equal for both models. For this choice of parameters, both models exhibit the same  $q = \pi$  lattice dimerization, where alternating bonds expand and contract along the length of the chain.

The equivalence between the aSSH and oSSH models in 1D may be expected by considering the various energies entering the respective Hamiltonians. The potential energy cost for this dimerization is identical for both models when  $\Omega_o(\pi) = \Omega_a(\pi)$ . The dimerization also couples to the electronic hopping integrals via the same microscopic  $e$ -ph interactions in both models. It is unsurprising that they produce similar physics in the weak-coupling limit when viewed in this light. Conversely, we found that the bSSH model differs significantly from the aSSH and oSSH models, which we attribute to the nonzero coupling to the  $q = 0$  phonon mode in the former case. This same coupling is also reflected in an overall contraction of the lattice observed in the bSSH model, which is forbidden in the aSSH and oSSH models.

Our results do not agree with Ref. [27], which found an equivalence between the bond and acoustic models at half-filling. The origin of this discrepancy is unclear, but we suspect it may be related to how that study treated the coupling to the  $q = 0$  modes in these models.

The equivalency here has been established only for the half-filled 1D model. Upon doping, we found that the acoustic and optical models agreed only qualitatively when we fixed the model parameters based on the Fermi surface of the half-filled model. We suspect it is possible to retain the consistency between the aSSH and oSSH models by adjusting the phonon dispersion and  $e$ -ph coupling value to reflect the Fermi momentum of the doped system. However, maintaining this equivalence in higher dimensions, where the Fermi surface may no longer be well nested, would be challenging. Additionally, we have found that in the bSSH model the coupling to the  $\mathbf{q} = 0$  mode in the bond model persists in our simulations of this model in 2D. Therefore, we expect this model to remain formally inequivalent to the optical and acoustic SSH models in higher dimensions. We conclude that the bond, optical,

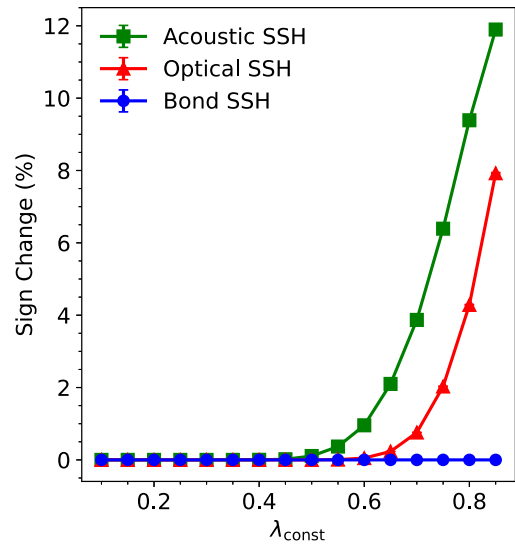


FIG. 9. The percentage number of times that the effective hopping integral changes sign during our DQMC simulations as a function of  $\lambda^{\text{const}}$ . Results were obtained on an  $L = 24$  site chain at an inverse temperature  $\beta = 15/t$  and a fixed  $\langle n \rangle = 1$  ( $\mu = 0.0$ ).

and acoustic variants of the SSH models are in general quite different models, and this aspect should be kept in mind when drawing broader conclusions from results obtained from one of these models.

#### ACKNOWLEDGMENTS

The authors thank M. Weber for useful discussions. This work was supported by the U.S. Department of Energy, Office of Science, Office of Basic Energy Sciences, under Award No. DE-SC0022311. This research used resources of the Oak Ridge Leadership Computing Facility, a DOE Office of Science User Facility supported under Contract No. DE-AC05-00OR22725.

#### APPENDIX A: SIGN CHANGES IN THE EFFECTIVE HOPPING INTEGRAL

The modulation of the hopping integrals by the lattice produces an effective hopping that now depends on the phonon displacement  $\hat{X}_{i,\nu}$  such that

$$t_{i,\nu}^{\text{a(o)}} = t - \alpha_{\text{a(o)}} \langle \hat{X}_{i+\mathbf{a},\nu} - \hat{X}_{i,\nu} \rangle, \quad \text{and} \\ t_{i,\nu}^{\text{b}} = t - \alpha_{\text{b}} \langle \hat{X}_{i,\nu} \rangle. \quad (\text{A1})$$

Crucially, the sign of the effective hopping can change in all three cases if the lattice displacements are large enough. These unphysical sign changes lead to dimerization via a mechanism utterly distinct from the standard Fermi-surface-nesting scenario, as discussed in Ref. [31]. Our HMC sampling procedure can produce lattice configurations where the sign of the hopping has changed. Therefore, we monitored the percentage of times this occurs in our simulations. Figure 9 presents results for a half-filled  $L = 24$  site chain as a function of  $\lambda^{\text{const}}$  and a fixed  $\beta = 15/t$ . Note that we do *not* average the phonon positions over imaginary time before calculating this percentage. The results indicate that the hopping integrals

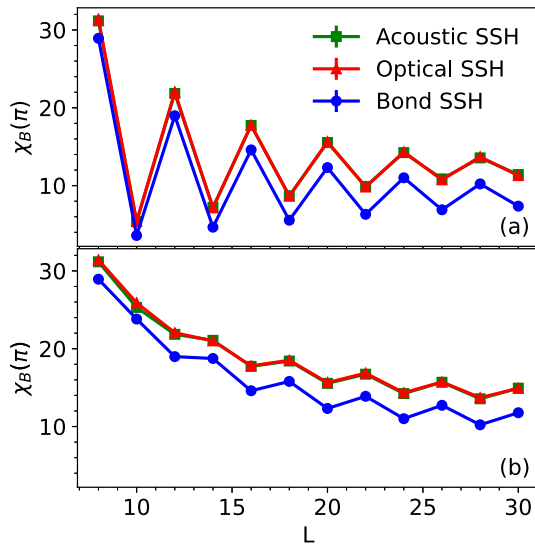


FIG. 10. The bond susceptibility  $\chi_B(q=\pi)$  at  $\langle n \rangle = 1$  ( $\mu = 0.0$ ) as a function of the chain length  $L$ . Results were obtained at an inverse temperature of  $\beta = 15.0$  and a fixed dimensionless coupling  $\lambda^{\text{const}} = 0.2$ . (a) Simulation result obtained using periodic boundary conditions for all lattice size. (b) Periodic boundary are replaced with aperiodic boundary conditions when the length of the chain  $L$  is not a multiple of four.

rarely change in our simulations for  $\lambda^{\text{const}} \leq 0.5$ . Some sign switching does occur in both the acoustic and optical models  $\lambda^{\text{const}} \gtrsim 0.6$ , however, it is still fairly rare in the DQMC simulations. For example, the aSSH model has a sign switching of

approximately 4% at  $\lambda^{\text{const}} = 0.7$ . Both the aSSH and oSSH models become more prone to these unphysical sign changes in the strong-coupling limit, while the bSSH model is not. We attribute this difference to the coupling to the  $q = 0$  mode in the latter case, which causes the entire lattice to contract, thus increasing  $|t_{i,v}^b|$ .

## APPENDIX B: FINITE-SIZE EFFECTS AT HALF-FILLING

Figure 10 presents the dependence of the bond susceptibility  $\chi_B(q=\pi)$  for a half-filled system as a function of chain length  $L$ . Results are shown for the aSSH, bSSH, and oSSH models for a fixed  $\beta = 15/t$  and  $\lambda^{\text{const}} = 0.2$ . In Fig. 10(a), where strictly periodic boundary conditions are used, we observe a clear oscillation in the value of  $\chi_B(q=\pi)$ . Expressing the length of the chain as  $L = 2n$  where  $n$  is an integer, the strength of the correlations are under- (over-)predicted relative to the thermodynamic limit whenever  $n$  is even (odd). The size of these oscillations, resulting from finite-size effects, can be reduced, but not entirely eliminated, by applying aperiodic boundary conditions when  $n$  is odd, as see in Fig. 10(b). This partially suppresses the finite-size effects because the aperiodic boundary conditions shift the noninteracting finite momentum grid when  $n$  is odd to include the Fermi surface points  $k = \pm \frac{\pi}{2}$  when  $\langle n \rangle = 1$ . Importantly, all three models exhibit the same oscillatory behavior with  $L$ , and both the aSSH and oSSH models produce identical values of  $\chi_B(\pi)$  for a given chain length. Thus, while our  $L = 24$  chains are short enough to retain some cluster size dependence, our conclusions on the equivalence of the three models will hold in the thermodynamic limit.

- [1] T. Holstein, Studies of polaron motion: Part I. The molecular-crystal model, *Ann. Phys.* **8**, 325 (1959).
- [2] H. Fröhlich, Electrons in lattice fields, *Adv. Phys.* **3**, 325 (1954).
- [3] S. Barišić, J. Labbé, and J. Friedel, Tight binding and transition-metal superconductivity, *Phys. Rev. Lett.* **25**, 919 (1970).
- [4] W. P. Su, J. R. Schrieffer, and A. J. Heeger, Solitons in polyacetylene, *Phys. Rev. Lett.* **42**, 1698 (1979).
- [5] J. K. Freericks, M. Jarrell, and D. J. Scalapino, Holstein model in infinite dimensions, *Phys. Rev. B* **48**, 6302 (1993).
- [6] A. J. Millis, R. Mueller, and B. I. Shraiman, Fermi-liquid-to-polaron crossover. II. Double exchange and the physics of colossal magnetoresistance, *Phys. Rev. B* **54**, 5405 (1996).
- [7] M. Capone, W. Stephan, and M. Grilli, Small-polaron formation and optical absorption in Su-Schrieffer-Heeger and Holstein models, *Phys. Rev. B* **56**, 4484 (1997).
- [8] R. T. Scalettar, N. E. Bickers, and D. J. Scalapino, Competition of pairing and Peierls-charge-density-wave correlations in a two-dimensional electron-phonon model, *Phys. Rev. B* **40**, 197 (1989).
- [9] E. Jeckelmann and S. R. White, Density-matrix renormalization-group study of the polaron problem in the Holstein model, *Phys. Rev. B* **57**, 6376 (1998).
- [10] M. Hohenadler, H. G. Evertz, and W. von der Linden, Quantum Monte Carlo and variational approaches to the Holstein model, *Phys. Rev. B* **69**, 024301 (2004).
- [11] G. De Filippis, V. Cataudella, A. S. Mishchenko, C. A. Perroni, and J. T. Devreese, Validity of the Franck-Condon principle in the optical spectroscopy: Optical conductivity of the Fröhlich polaron, *Phys. Rev. Lett.* **96**, 136405 (2006).
- [12] P. Werner and A. J. Millis, Efficient dynamical mean field simulation of the Holstein-Hubbard model, *Phys. Rev. Lett.* **99**, 146404 (2007).
- [13] F. F. Assaad and T. C. Lang, Diagrammatic determinantal quantum Monte Carlo methods: Projective schemes and applications to the Hubbard-Holstein model, *Phys. Rev. B* **76**, 035116 (2007).
- [14] G. L. Goodvin, A. S. Mishchenko, and M. Berciu, Optical conductivity of the Holstein polaron, *Phys. Rev. Lett.* **107**, 076403 (2011).
- [15] F. Grusdt, Y. E. Shchadilova, A. N. Rubtsov, and E. Demler, Renormalization group approach to the Fröhlich polaron model: application to impurity-BEC problem, *Sci. Rep.* **5**, 12124 (2015).
- [16] M. Weber, F. F. Assaad, and M. Hohenadler, Phonon spectral function of the one-dimensional Holstein-Hubbard model, *Phys. Rev. B* **91**, 235150 (2015).
- [17] J. Greitemann and L. Pollet, Lecture notes on Diagrammatic Monte Carlo for the Fröhlich polaron, *SciPost Phys. Lect. Notes* **2** (2018).
- [18] I. Esterlis, B. Nosarzewski, E. W. Huang, B. Moritz, T. P. Devreux, D. J. Scalapino, and S. A. Kivelson,

- Breakdown of the Migdal-Eliashberg theory: A determinant quantum Monte Carlo study, *Phys. Rev. B* **97**, 140501(R) (2018).
- [19] S. Karakuzu, K. Seki, and S. Sorella, Solution of the sign problem for the half-filled Hubbard-Holstein model, *Phys. Rev. B* **98**, 201108(R) (2018).
- [20] M. Weber and M. Hohenadler, Two-dimensional Holstein-Hubbard model: Critical temperature, Ising universality, and bipolaron liquid, *Phys. Rev. B* **98**, 085405 (2018).
- [21] J. Bonča, S. A. Trugman, and M. Berciu, Spectral function of the Holstein polaron at finite temperature, *Phys. Rev. B* **100**, 094307 (2019).
- [22] P. M. Dee, J. Coulter, K. G. Kleiner, and S. Johnston, Relative importance of nonlinear electron-phonon coupling and vertex corrections in the Holstein model, *Commun. Phys.* **3**, 145 (2020).
- [23] O. Bradley, G. G. Batrouni, and R. T. Scalettar, Superconductivity and charge density wave order in the two-dimensional Holstein model, *Phys. Rev. B* **103**, 235104 (2021).
- [24] A. Götz, M. Hohenadler, and F. F. Assaad, Phases and exotic phase transitions of a two-dimensional Su-Schrieffer-Heeger model, [arXiv:2307.07613](https://arxiv.org/abs/2307.07613).
- [25] R. Peierls, *More Surprises in Theoretical Physics* (Princeton University Press, Princeton, 1992).
- [26] P. Sengupta, A. W. Sandvik, and D. K. Campbell, Peierls transition in the presence of finite-frequency phonons in the one-dimensional extended Peierls-Hubbard model at half-filling, *Phys. Rev. B* **67**, 245103 (2003).
- [27] M. Weber, F. F. Assaad, and M. Hohenadler, Excitation spectra and correlation functions of quantum Su-Schrieffer-Heeger models, *Phys. Rev. B* **91**, 245147 (2015).
- [28] J. Sous, M. Chakraborty, R. V. Krems, and M. Berciu, Light bipolarons stabilized by Peierls electron-phonon coupling, *Phys. Rev. Lett.* **121**, 247001 (2018).
- [29] C. Zhang, J. Sous, D. R. Reichman, M. Berciu, A. J. Millis, N. V. Prokof'ev, and B. V. Svistunov, Bipolaronic high-temperature superconductivity, *Phys. Rev. X* **13**, 011010 (2023).
- [30] A. Nocera, J. Sous, A. E. Feiguin, and M. Berciu, Bipolaron liquids at strong Peierls electron-phonon couplings, *Phys. Rev. B* **104**, L201109 (2021).
- [31] D. Banerjee, J. Thomas, A. Nocera, and S. Johnston, Ground-state and spectral properties of the doped one-dimensional optical Hubbard-Su-Schrieffer-Heeger model, *Phys. Rev. B* **107**, 235113 (2023).
- [32] S. Li and S. Johnston, Suppressed superexchange interactions in the cuprates by bond-stretching oxygen phonons, [arXiv:2205.12678](https://arxiv.org/abs/2205.12678).
- [33] S. Li and S. Johnston, Quantum Monte Carlo study of lattice polarons in the two-dimensional three-orbital Su-Schrieffer-Heeger model, *npj Quantum Mater.* **5**, 40 (2020).
- [34] B. Xing, W.-T. Chiu, D. Poletti, R. T. Scalettar, and G. Batrouni, Quantum Monte Carlo simulations of the 2D Su-Schrieffer-Heeger model, *Phys. Rev. Lett.* **126**, 017601 (2021).
- [35] B. Cohen-Stead, K. Barros, R. Scalettar, and S. Johnston, A hybrid Monte Carlo study of bond-stretching electron-phonon interactions and charge order in BaBiO<sub>3</sub>, *npj Comput. Mater.* **9**, 40 (2023).
- [36] C. Feng, B. Xing, D. Poletti, R. Scalettar, and G. Batrouni, Phase diagram of the Su-Schrieffer-Heeger-Hubbard model on a square lattice, *Phys. Rev. B* **106**, L081114 (2022).
- [37] X. Cai, Z.-X. Li, and H. Yao, Robustness of antiferromagnetism in the Su-Schrieffer-Heeger Hubbard model, *Phys. Rev. B* **106**, L081115 (2022).
- [38] E. J. Meier, F. A. An, and B. Gadway, Observation of the topological soliton state in the Su-Schrieffer-Heeger model, *Nat. Commun.* **7**, 13986 (2016).
- [39] M. M. Möller, G. A. Sawatzky, M. Franz, and M. Berciu, Type-II Dirac semimetal stabilized by electron-phonon coupling, *Nat. Commun.* **8**, 2267 (2017).
- [40] S. Bid and A. Chakrabarti, Topological properties of a class of Su-Schrieffer-Heeger variants, *Phys. Lett. A* **423**, 127816 (2022).
- [41] M. Hohenadler and T. C. Lang, Autocorrelations in quantum Monte Carlo simulations of electron-phonon models, in *Computational Many-Particle Physics*, edited by H. Fehske, R. Schneider, and A. Weiße (Springer, Berlin, 2008) pp. 357–366.
- [42] S. Beyl, F. Goth, and F. F. Assaad, Revisiting the hybrid quantum Monte Carlo method for Hubbard and electron-phonon models, *Phys. Rev. B* **97**, 085144 (2018).
- [43] G. G. Batrouni and R. T. Scalettar, Langevin simulations of a long-range electron-phonon model, *Phys. Rev. B* **99**, 035114 (2019).
- [44] S. Duane, A. Kennedy, B. J. Pendleton, and D. Roweth, Hybrid Monte Carlo, *Phys. Lett. B* **195**, 216 (1987).
- [45] B. Cohen-Stead, O. Bradley, C. Miles, G. Batrouni, R. Scalettar, and K. Barros, Fast and scalable quantum Monte Carlo simulations of electron-phonon models, *Phys. Rev. E* **105**, 065302 (2022).
- [46] B. Cohen-Stead, K. Barros, Z. Y. Meng, C. Chen, R. T. Scalettar, and G. G. Batrouni, Langevin simulations of the half-filled cubic Holstein model, *Phys. Rev. B* **102**, 161108(R) (2020).
- [47] O. Bradley, B. Cohen-Stead, S. Johnston, K. Barros, and R. T. Scalettar, Charge order in the kagome lattice Holstein model: A hybrid Monte Carlo study, *npj Quantum Mater.* **8**, 21 (2023).
- [48] C. Zhang, N. V. Prokof'ev, and B. V. Svistunov, Peierls/Su-Schrieffer-Heeger polarons in two dimensions, *Phys. Rev. B* **104**, 035143 (2021).
- [49] Z. Li, C. J. Chandler, and F. Marsiglio, Perturbation theory of the mass enhancement for a polaron coupled to acoustic phonons, *Phys. Rev. B* **83**, 045104 (2011).
- [50] P. B. Allen and B. Mitrović, *Theory of superconducting T<sub>c</sub>* (Academic Press, New York, 1983), pp. 1–92.
- [51] J. P. Carbotte, Properties of boson-exchange superconductors, *Rev. Mod. Phys.* **62**, 1027 (1990).
- [52] S. R. White, D. J. Scalapino, R. L. Sugar, E. Y. Loh, J. E. Gubernatis, and R. T. Scalettar, Numerical study of the two-dimensional Hubbard model, *Phys. Rev. B* **40**, 506 (1989).
- [53] A. Götz, S. Beyl, M. Hohenadler, and F. F. Assaad, Valence-bond solid to antiferromagnet transition in the two-dimensional Su-Schrieffer-Heeger model by Langevin dynamics, *Phys. Rev. B* **105**, 085151 (2022).
- [54] N. S. Nichols, P. Sokol, and A. Del Maestro, Parameter-free differential evolution algorithm for the analytic continuation of



- imaginary time correlation functions, [Phys. Rev. E \*\*106\*\*, 025312 \(2022\)](#).
- [55] C. Miles, B. Cohen-Stead, O. Bradley, S. Johnston, R. Scalettar, and K. Barros, Dynamical tuning of the chemical potential to achieve a target particle number in grand canonical Monte Carlo simulations, [Phys. Rev. E \*\*105\*\*, 045311 \(2022\)](#).
- [56] S. Engelsberg and J. R. Schrieffer, Coupled electron-phonon system, [Phys. Rev. \*\*131\*\*, 993 \(1963\)](#).
- [57] B. Nosarzewski, M. Schüler, and T. P. Devereaux, Spectral properties and enhanced superconductivity in renormalized Migdal-Eliashberg theory, [Phys. Rev. B \*\*103\*\*, 024520 \(2021\)](#).